Robotica: (2021) volume 39, pp. 1617–1633. © The Author(s), 2021. Published by Cambridge University Press.
doi:10.1017/S0263574720001393

Feasible Arm Configurations and its Application for Human-Like Motion Control of S-R-S-Redundant Manipulators with Multiple Constraints

Jing Xia†, Zai-nan Jiang‡*, Ting Zhang¶

†*School of Mechanical Engineering, Xi'an University of Science and Technology, Xi'an, China*
‡*State Key Laboratory of Robotics and System, Harbin Institute of Technology, Harbin, China*
¶*Robotics and Microsystems Center, College of Mechanical and Electrical Engineering, Soochow University, Suzhou, China*

(Accepted December 12, 2020. First published online: February 1, 2021)

SUMMARY
This paper presents a general framework for human-like motion control of 7-DOF S-R-S-redundant manipulators. The new framework simultaneously accomplishes five objectives: Cartesian trajectory tracking, obstacle avoidance, joint limit avoidance, human-like movement, and a feasibility evaluation of the Cartesian trajectory. We exhaustively compute all feasible arm configurations. This allows for quick evaluations of the feasibility of the Cartesian trajectories. They are applied to inverse kinematics of the redundant manipulator to improve the capability to handle multiple constraints, and enable the manipulator to imitate human movements. The efficiency of the proposed framework is demonstrated by kinematic experiments with a humanoid robot.

KEYWORDS: Redundant manipulators; Serial manipulator; Design and kinematics; Motion planning; Control of robotic systems; Humanoid robots.

1. Introduction

Redundant manipulators have been employed increasingly more often to accomplish human–robot collaboration tasks, such as disaster relief, spacecraft logistics, and home caretaking.[1,2] The 7-DOF spherical-revolute-spherical (S-R-S)-redundant manipulator is being studied increasingly more often because the manipulator has a structure and level of dexterity that are similar to those of a human arm and is widely used as a humanoid's arm, as shown in Fig. 1. One of the main difficulties in using the redundant manipulator for human–robot collaboration is the transparency between the operator and the manipulator. The operators can, at all times, feel confident that they understand the robot's intentions and intuitively control the redundant manipulator if the manipulator has human-like structural and movement characteristics. For a human arm, when given a desired Cartesian trajectory, people instinctively evaluate the feasibility of this trajectory and adopt a certain underlying strategy to select the best joint trajectories for fine control while simultaneously avoiding joint motion limits and collisions. However, it is very challenging to enable redundant manipulators to perform human-like movements by using current existing trajectory feasibility evaluation methods and inverse kinematics.

The methods that have previously been used to evaluate the feasibility of Cartesian trajectories include a workspace analysis and inverse kinematics. Various methods for computing the workspace have been proposed,[3–9] such as a geometric analysis,[3] an optimization approach,[4] the Monte Carlo

* Corresponding author. E-mail: jiangzainan@hit.edu.cn

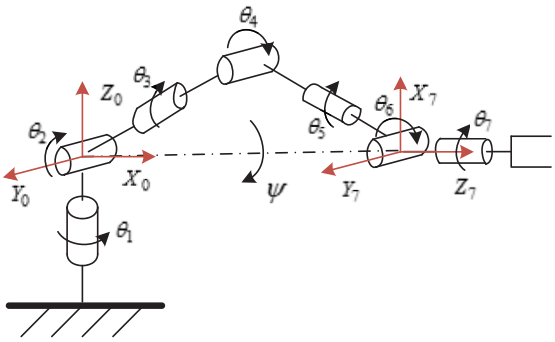

Fig. 1. The spherical-revolute-spherical (S-R-S)-redundant manipulator.

method,[5,6] and a polynomial discriminant.[7] However, the workspace analysis-based methods mainly focus on the determination of the maximum workspace. The feasibility of the trajectory cannot be determined when the orientation of the manipulator tips is taken into account, even if it lies entirely in the maximum workspace. It is essential for the workspace to include orientation information, but the description of this workspace is considerably complicated and difficult.[10] Due to the redundancy characteristic of the manipulator, it would be difficult or impractical to use inverse kinematics to analyze the feasibility of the Cartesian trajectories of redundant manipulators; thus, a new evaluation method needs to be developed.

Various methods have been used to imitate human-like motion based on human-like optimization criteria and the inverse kinematic (IK) computations for 7-DOF-redundant manipulators with multiple constraints. Previous studies have proposed several optimization criteria to achieve a unique human-like solution, such as the optimization criteria that combined both kinematic and dynamic criteria,[11] the energy-related criterion that included gravitational potential and kinetic energies of the arm,[12,13] the rapid upper limb assessment (RULA)[14] criterion from ergonomic research, the criterion that minimized the magnitude of total work performed by joint torques,[15] a task-driven muscular effort minimization criterion, and the manipulability ellipsoid optimization criterion.[16] Other strategies include developing a mathematical model or extracting features from human arm kinematics for human-like control.[17–19] But these studies usually do not consider obstacle avoidance and joint limits.

The inverse kinematic (IK) computations for 7-DOF-redundant manipulators can be classified into two types, namely velocity-based and position-based methods. The velocity-based method iteratively calculates a velocity-based inverse solution by using the Jacobian matrix. Generally, it involves calculating the pseudoinverse,[20] the gradient projection method (GPM),[21] the damped least squares,[22] and the weighted least-norm ones.[23] However, these methods cannot be applied when the number of constraints is larger than the degrees of redundancy. More advanced IK approaches, such as the task-priority redundancy resolution technique,[24] hierarchical formalisms,[25] the general-weighted least-norm (GWLN) method,[26] and the varied weights (VW) method,[27] have been proposed to cope with the joint limits and the collision constraints. Vahrenkamp[28] developed the IK-Map approach to improve the success rate, performance, and quality of the resulting IK solutions while considering the joint limits and collision constraints. However, it is difficult to explicitly describe the null space with velocity-based approaches;[33] they are not suitable for the Cartesian trajectory analysis of redundant manipulators.

Compared with the velocity-based method, the position-based method is characterized by improved accuracy and a lower computational cost, and the position-based method can derive the closed-form inverse kinematic solution of 7-DOF-redundant manipulators. Several approaches to solving the inverse kinematic problem in the position domain have been developed, such as the joint parameter-based method,[29] redundancy circle parameter method,[30,31] arm angle approach,[32,33] and movement primitives-based approach.[34] Dahm[30] and Moradi[31] analyzed the limitation of the redundancy circle parameter for the wrist joint limits and the shoulder joint limits, respectively. Shimizu[33] developed a method for identifying all the feasible arm configurations under joint limits. Lück[35]

https://doi.org/10.1017/S0263574720001393 Published online by Cambridge University Press

studied the topological properties of self-motion in a global configuration space constrained by joint limits. However, these methods have not considered obstacle avoidance and human-like motion. For a redundant manipulator with such partial orientation constraints, Liu[36] presented an analytical inverse kinematics solver that could generate human-like motion while satisfying joint limits and obstacle avoidance criteria. This approach has some similarity to the one presented here, but it avoids joint limits and obstacles by iteratively adjusting the robot key positions and the wrist position. In recent years, quadratic programming approaches synthesized by recurrent neural networks have been widely used to address this issue.[37,38] However, the limitations of the methods include the difficulty of handling multi-objective optimization, the computational intensity, and there is a lack of an effective scheme to combine the human-like optimization criteria and the inverse kinematic with multiple constraints.

Building on the previously mentioned research, this paper presents a general unifying framework for human-like motion control of 7-DOF S-R-S-redundant manipulators with multiple constraints, which gives the manipulator human-like motion characteristics. The new framework inherits the high precision of the position-based method and simultaneously accomplishes five objectives: Cartesian trajectory tracking, obstacle avoidance, joint limit avoidance, human-like movement, and a feasibility evaluation of the Cartesian trajectory. In this framework, we exhaustively compute all feasible arm configurations of 7-DOF S-R-S-redundant manipulators with multiple constraints. This allows for quick evaluations of the feasibility of the desired trajectories. The feasible arm configurations are applied to inverse kinematics of 7-DOF-redundant manipulators to improve the capability to handle multiple constraints and enable the manipulator to imitate human movements. This feasible arm configuration architecture can serve as a framework in the future for the development of an S-R-S-redundant manipulator human–robot collaboration system to allow the operators to intuitively control the redundant manipulator and confidently understand the manipulator's intentions.

This study includes the following major contributions:

- We proposed a framework that defines a feasible arm configuration to represent the self-motion manifold of an S-R-S-redundant manipulator with multiple constraints at a particular end-effector pose. Then, a real-time method for computing feasible arm configurations has been proposed.
- To our knowledge, this is the first study to use the feasible arm configurations to quickly evaluate the feasibility of the Cartesian trajectory of 7-DOF-redundant manipulators under multiple constraints.
- The redundancy resolution problem of 7-DOF-redundant manipulators with multiple constraints is simplified to a 1D optimization problem in the proposed framework, which will significantly reduce the difficulty of the algorithm and realize human-like redundancy resolution optimization with multiple constraints.

2. Human-like Motion Control Framework of Redundant Manipulators with Multiple Constraints

A general unifying framework for human-like motion control of 7-DOF S-R-S-redundant manipulators with multiple constraints is proposed in this section, as shown in Fig. 2. The inputs of this framework are a Cartesian trajectory, joint limits, a robot, and the surrounding environment models. Finally, the outputs are human-like joint angles satisfying the joint limits and obstacle avoidance criteria. The framework is composed of three main components: a description of the feasible arm configurations, a feasibility evaluation of the Cartesian trajectory, and human-like redundancy resolution optimization.

Regarding the kinematics, the human-like motion control problem of a 7-DOF-redundant manipulator with multiple constraints is described generally by

$$\begin{aligned} &\max \quad c = opt(\theta(t)) \\ &s.t. \begin{cases} fk(\theta(t)) = x^d \\ \theta^l \le \theta \le \theta^u \\ dis(\theta(t)) \ge 0 \end{cases}, \end{aligned} \tag{1}$$

https://doi.org/10.1017/S0263574720001393 Published online by Cambridge University Press

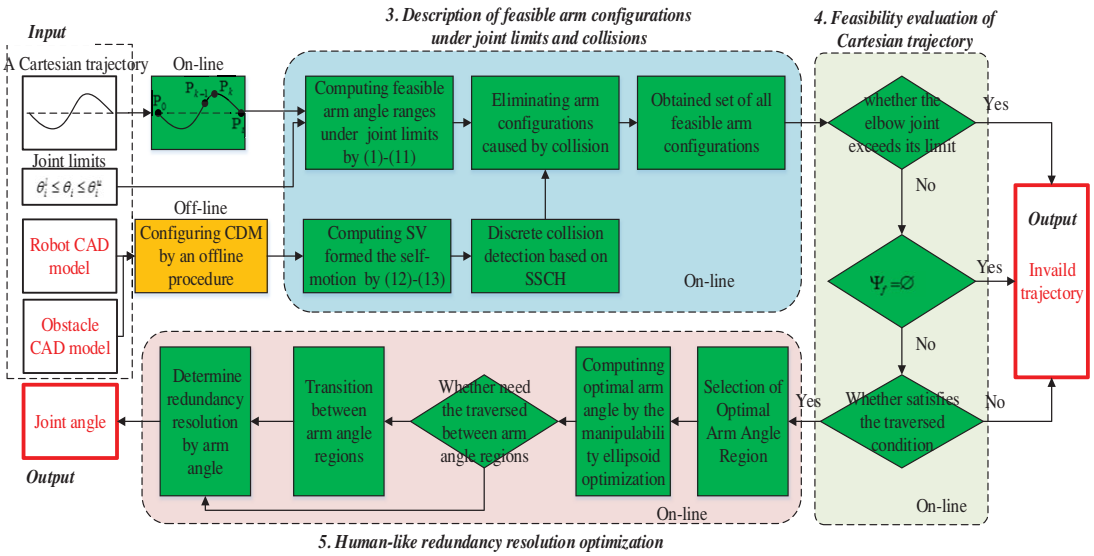

Fig. 2. A novel framework for human-like motion control of the S-R-S-redundant manipulator with multiple constraints.

where $opt(\theta(t))$ is the human-like optimization function; $fk(\theta(t))$ denotes the forward kinematics of the redundant manipulator; x^d is the desired tip pose; θ^l and θ^u are the lower and upper bounds of the joint θ, respectively; and $dis(\theta(t))$ denotes the nearest distances of collision check pairs. The challenge is identifying a group of optimal joint angles in the 7D joint space constrained by 6 equalities and a large number of inequalities (containing 14 inequalities of joint limits and dozens or even hundreds of inequalities denoting collision check pairs). In most cases, solving this problem is extremely difficult. In the new framework, the problem can be simplified to a 1D optimization problem by using the feasible arm configurations.

3. Description of Feasible Arm Configurations under Multiple Constraints

The S-R-S-redundant manipulator can yield a self-motion around the axis connecting the shoulder and wrist. Self-motion is subject to joint limits and collisions, and not all the arm configurations are feasible. In this paper, a feasible arm configuration is defined as a configuration that represents the self-motion manifold of the S-R-S-redundant manipulator with multiple constraints at a particular end-effector pose.

3.1. Joint limits

The desired tip position and orientation are specified by ${}^0x_7$ and ${}^0R_7$, respectively. The ranges of motion of the ith joint are represented by

$$-\pi \le \theta_i^l \le \theta_i \le \theta_i^u \le \pi, \tag{2}$$

where θ_i^l and θ_i^u are the lower and upper bounds of the joint, respectively. In this paper, the feasible arm configurations of the redundant manipulator under joint limits are obtained by directly solving the inequality of joint limits and the arm angle.

3.1.1. Feasible arm configurations for cosine function. The kinematic equations of joint 2 and joint 6 are generally represented by the cosine function.[33]

$$\cos\theta_i = a\sin\psi_i + b\cos\psi_i + c \ (i = 2, 6) \tag{3}$$

when $i = 2$, a, b and c are the (3, 2) elements of the matrices A_s, B_s and C_s, respectively. A_s, B_s and C_s are constant matrices given by

$$A_s = -\left[{}^0u_{sw}\times\right]{}^0R_3^o,\ B_s = \left[{}^0u_{sw}\times\right]^2{}^0R_3^o,\ C_s = -\left[{}^0u_{sw}\,{}^0u_{sw}^T\right]^2, \tag{4}$$

https://doi.org/10.1017/S0263574720001393 Published online by Cambridge University Press

where ${}^0u_{sw} \in R^3$ is the unit vector of ${}^0x_7$, $[{}^0u_{sw}\times]$ is the skew-symmetric matrix of the vector ${}^0u_{sw}$, ${}^iR_j$ is the rotation matrix of the coordinate system Σ_j viewed from the coordinate systems Σ_i, and ${}^0R_3^o$ is the rotation matrix between the coordinate systems Σ_0 and Σ_3 when the arm angle is zero. When $i = 6$, a, b and c are the (3, 3) elements of the matrices A_w, B_w and C_w, respectively. A_w, B_w and C_w are constant matrices given by

$$A_w = {}^3R_4^T A_s^T {}^0R_7,\ B_w = {}^3R_4^T B_s^T {}^0R_7,\ C_w = {}^3R_4^T C_s^T {}^0R_7. \tag{5}$$

To construct the inequality of the joint limits and the arm angle, the ranges of the whole joint motion are separated into two regions, $\theta_i \in [\theta_i^l, 0]$ and $\theta_i \in [0, \theta_i^u]$. The feasible arm configurations Ψ_i^- in the region $[\theta_i^l, 0]$ are calculated by using

$$\cos\theta_i^l \le a\sin\Psi_i^- + b\cos\Psi_i^- + c \le 1\ (i = 2, 6)\,. \tag{6}$$

The feasible arm configurations Ψ_i^+ in the region $[0, \theta_i^u]$ are given by

$$\cos\theta_i^u \le a\sin\Psi_i^+ + b\cos\Psi_i^+ + c \le 1\ (i = 2, 6)\,. \tag{7}$$

Thus, all the feasible arm configurations satisfying the joint limits are identified by

$$\Psi_i = \Psi_i^- \bigcup \Psi_i^+\ (i = 2, 6)\,. \tag{8}$$

3.1.2. Feasible arm configurations for tangent function. The kinematic equations of joint 1, joint 3, joint 5, and joint 7 are represented generally by the tangent function.[33]

$$\tan\theta_j = \frac{sign(\sin\theta_i)(a_n\sin\Psi_j + b_n\cos\Psi_j + c_n)}{sign(\sin\theta_i)(a_d\sin\Psi_j + b_d\cos\Psi_j + c_d)}\ \begin{matrix}(i = 2, 6,\\ j = 1, 3, 5, 7)\end{matrix}, \tag{9}$$

where $a_n, b_n, c_n, a_d, b_d,$ and c_d are the corresponding elements of the matrices A_s, B_s, C_s, A_w, B_w and C_w, respectively.

Since the tangent function is a cyclic function, one-to-one correspondence between the joint angle and the arm angle is not ensured in $[-\pi, \pi]$, and ranges of the joint must be divided into several monotonic regions. For example, for $\theta_j^l \in [-\pi/2, 0]$ and $\theta_j^u \in [\pi/2, \pi]$, the ranges of motion are separated into two monotonic regions $[\theta_j^l, \pi/2]$ and $[\pi/2, \theta_j^u]$. In region I $\theta_j \in [\theta_j^l, \pi/2]$, the tangent function is monotonic and continuous, and its denominator must be larger than zero. The inequalities between the arm angle and the joint limit are constructed as follows

$$\begin{cases} (a_d\sin\Psi_{j\mathrm{I}} + b_d\cos\Psi_{j\mathrm{I}} + c_d)sign(\sin\theta_i) > 0 \\ \tan\theta_j^l < \dfrac{(a_n\sin\Psi_{j\mathrm{I}} + b_n\cos\Psi_{j\mathrm{I}} + c_n)sign(\sin\theta_i)}{(a_d\sin\Psi_{j\mathrm{I}} + b_d\cos\Psi_{j\mathrm{I}} + c_d)sign(\sin\theta_i)}\,. \end{cases} \tag{10}$$

It can be seen that the arm angle satisfying the inequalities depends on the sign of θ_i; thus, the feasible arm configurations are given by

$$\Psi_{j\mathrm{I}} = \Psi_{j\mathrm{I}}^- \bigcup \Psi_{j\mathrm{I}}^+, \tag{11}$$

where $\Psi_{j\mathrm{I}}^-$ and $\Psi_{j\mathrm{I}}^+$ are the corresponding solutions of the inequalities when $\theta_i \in [\theta_i^l, 0]$ and $\theta_i \in [0, \theta_i^u]$, respectively.

In region II, $\theta_j \in [\pi/2, \theta_j^u]$, the tangent function is also monotonic and continuous, its numerator is larger than zero, and its denominator is less than zero. The feasible arm configurations $\Psi_{j\mathrm{II}}$ in this region are computed by the inequalities.

$$\begin{cases} (a_n\sin\Psi_{j\mathrm{II}} + b_n\cos\Psi_{j\mathrm{II}} + c_n)sign(\sin\theta_i) > 0 \\ \dfrac{(a_n\sin\Psi_{j\mathrm{II}} + b_n\cos\Psi_{j\mathrm{II}} + c_n)sign(\sin\theta_i)}{(a_d\sin\Psi_{j\mathrm{II}} + b_d\cos\Psi_{j\mathrm{II}} + c_d)sign(\sin\theta_i)} < \tan\theta_j^u\,. \\ (a_d\sin\Psi_{j\mathrm{II}} + b_d\cos\Psi_{j\mathrm{II}} + c_d)sign(\sin\theta_i) < 0 \end{cases} \tag{12}$$

https://doi.org/10.1017/S0263574720001393 Published online by Cambridge University Press

The feasible arm configurations in the region are also given by

$$\Psi_{j\mathrm{II}} = \Psi_{j\mathrm{II}}^{-} \bigcup \Psi_{j\mathrm{II}}^{+}, \tag{13}$$

where $\Psi_{j\mathrm{II}}^{-}$and $\Psi_{j\mathrm{II}}^{+}$are the corresponding solutions of the inequalities (12) when $\theta_i \in [\theta_i^l, 0]$ and $\theta_i \in [0, \theta_i^u]$, respectively.

Finally, all feasible arm configurations of the *j*th joint are expressed by

$$\Psi_j = \Psi_{j\mathrm{I}} \cup \Psi_{j\mathrm{II}} = \Psi_{j\mathrm{I}}^{-} \cup \Psi_{j\mathrm{I}}^{+} \cup \Psi_{j\mathrm{II}}^{-} \cup \Psi_{j\mathrm{II}}^{+} = (\Psi_{j\mathrm{I}}^{-} \cup \Psi_{j\mathrm{II}}^{-}) \cup (\Psi_{j\mathrm{I}}^{+} \cup \Psi_{j\mathrm{II}}^{+}) = \Psi_j^{-} \cup \Psi_j^{+}, \tag{14}$$

where $\Psi_j^{-}$and $\Psi_j^{+}$are the corresponding feasible arm configurations of the *j*th joint limit when $\theta_i < 0$ and $\theta_i > 0$, respectively. For the ranges of different joint motion, different inequality cases can be obtained in the same way and are not presented in detail here.

3.1.3. Feasible arm configurations under joint limits. Since all joint limits must be satisfied simultaneously, the feasible arm configurations for whole manipulator are described by Eq. (15). According to the sign of joint 2 and joint 6, we define four-arm configuration regions Ψ_{rk}^{L} $(k = 1, 2 \cdots, 4)$ to represent all the feasible arm configurations. In each arm configuration region, the relations between the arm angle and the inverse solutions have one-to-one relations, which is favorable for determining the inequalities and the kinematic control of redundant manipulators. Compared with the previous method, the method proposed here is much simpler and more efficient because it does not require the differentiation and analysis of the stationary points.

$$\begin{aligned}
\Psi^L &= \bigcup_{i=1}^{7} \Psi_i = \left(\Psi_1^{-} \cup \Psi_1^{+}\right) \cap \left(\Psi_2^{-} \cup \Psi_2^{+}\right) \cap \cdots \cap \left(\Psi_7^{-} \cup \Psi_7^{+}\right) \\
&= \left(\underbrace{\Psi_1^{-} \cap \Psi_2^{-} \cap \Psi_3^{-} \cap \Psi_5^{-} \cap \Psi_6^{-} \cap \Psi_7^{-}}_{\Psi_{r1}^{L}} \right) \cup \left(\underbrace{\Psi_1^{-} \cap \Psi_2^{-} \cap \Psi_3^{-} \cap \Psi_5^{+} \cap \Psi_6^{+} \cap \Psi_7^{+}}_{\Psi_{r2}^{L}} \right) \\
&\cup \left(\underbrace{\Psi_1^{+} \cap \Psi_2^{+} \cap \Psi_3^{+} \cap \Psi_5^{-} \cap \Psi_6^{-} \cap \Psi_7^{-}}_{\Psi_{r3}^{L}} \right) \cup \left(\underbrace{\Psi_1^{+} \cap \Psi_2^{+} \cap \Psi_3^{+} \cap \Psi_5^{+} \cap \Psi_6^{+} \cap \Psi_7^{+}}_{\Psi_{r4}^{L}} \right)
\end{aligned} \tag{15}$$

3.2. Collisions and self-collisions

Collisions are also an important factor affecting the feasible arm configurations. For the redundant manipulator, discrete collision detection approaches[39] require multiple discrete sampling for arm configurations, leading to a considerable computational cost. However, with continuous collision detection approaches,[40,41] it is difficult to describe the swept volumes (SVs) formed by all the arm configurations in every control interval. Thus, we propose an approximate and fast collision detection method to remove the arm configurations that are likely to collide with the environment or self-structure.

In the initial stage, we build the collision detection model of the manipulator using the sphere-swept line (SSL). For the rest of the robot and obstacles, sphere-swept convex hulls (SSCHs) are used to construct their collision detection models. The SSL and SSCHs are pre-computed by using an offline volume optimization procedure. They contain all points from the CAD model in the lowest possible volume, see Fig. 3(a).

At runtime, the approximate SVs formed by the feasible arm configurations under joint limits are computed by calculating the SVs of SSL, which encloses the links of the manipulator, as shown in Fig. 3(b). Supposing that the *k*-th arm configuration region is described as $\Psi_{rk}^{L} = [\psi^{l1}, \psi^{l2}]$, the non-convex SVs generated byΨ_{rk}^{L} must be split into several convex subparts to perform the approximation because the collision detection algorithm proposed here is only applicable to convex bodies.

https://doi.org/10.1017/S0263574720001393 Published online by Cambridge University Press

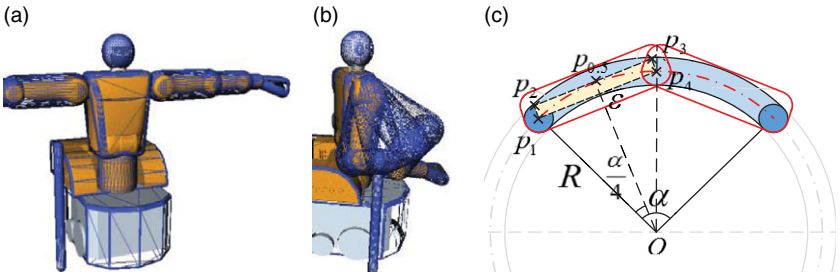

Fig. 3. (a) CAD model of humanoid robot and its collision detection model at the preprocess. (b) SV model formed by all feasible arm configurations under joint limits at runtime. (c) A tighter bound of the elbow trajectory is obtained by using two SSCH with four points.

As shown in Fig. 3(c), the parameterε identifies the maximum allowable error, and the number n of the convex subparts is the minimum value $n = \min\{1, 2, 3, ...\}$ that satisfies the following equation:

$$\begin{cases} \varepsilon \geq (1 - \cos(\alpha/2n))\,|R - r| \quad \forall n \in \{1, 2, 3, ...\} \\ \alpha = \psi^{l2} - \psi^{l1} \end{cases}, \tag{16}$$

where R is the distance from point O to point p_1 and r is the radius of the SSCH. The motion trajectory of the elbow is contained in two SSCHs. Each SSCH is composed of a radius and four vertices. Thus, the SVs generated by the SSL $V(r, \{p_i\}_{i=0}^{1})$ of the lower arm is formulated as

$$\begin{cases} SV(\Psi_{r1}^{L}, (r, \{p_i\}_{i=0}^{1})) \subset V_1(r, \{p_0, \{p_i\}_{i=1}^{4}\}) + V_2(r, \{p_0, \{p_i\}_{i=4}^{7}\}) \\ p_2 = p_1 + (1 - \cos(\alpha/2n))op_{0.5} \\ p_3 = p_4 + (1 - \cos(\alpha/2n))op_{0.5} \end{cases}, \tag{17}$$

where $V_1(r, \{p_0, \{p_i\}_{i=1}^{4}\})$ is the SSCH composed of radius r and a set of vertices$\{p_0, \{p_i\}_{i=1}^{4}\}$; $V_2(r, \{p_0, \{p_i\}_{i=4}^{7}\})$ is the SSCH composed of radius r and a set of vertices $\{p_0, \{p_i\}_{i=4}^{7}\}$; $p_{0.5}$ is the position of the vertex p_1 when the arm angle is $\alpha/2n$, and p_4 is the position of the vertex p_1 when the arm angle is α/n. Likewise, the five vertices of $V_2(r, \{p_0, \{p_i\}_{i=4}^{7}\})$ can also be computed.

Then, the collision check pairs are constructed between the swept volumes of the self-motion and the collision detection models, and the nearest distance and potential contact points of each collision check pair are computed by using the Gilbert–Johnson–Keerthi (GJK) algorithm. The GJK algorithm is an efficient and reliable iterative algorithm for computing the Euclidean distance between a pair of convex hulls. When the Euclidean distance is less than zero, the collision check pair collides. The inner primitives of the SSCH are convex hulls; thus, GJK is easily adopted for the SSCH. Once these unfeasible arm configurations are obtained, we eliminate them from the set of feasible arm configurations. For example, in the kth arm configuration region, the unfeasible arm configurations caused by collisions are $\Psi_{rk}^{C} = [\psi^{c1}, \psi^{c2}]$, feasible arm configurations are

$$\Psi_{r}^{L} - \Psi_{rk}^{C} = \left[\psi^{l1}, \psi^{c1}\right] \bigcup \left[\psi^{c2}, \psi^{l2}\right]. \tag{18}$$

Finally, all feasible arm configurations Ψ_f satisfying the joint limits and collision avoidance criteria are formulated as

$$\Psi_f = \bigcup_{k=1}^{4} \left(\Psi_{rk}^{L} - \Psi_{rk}^{C}\right) = \bigcup_{k=1}^{4} \Psi_{rk}. \tag{19}$$

From the above description, it can be seen that the proposed approach combines discrete collision detection and continuous collision detection. The new method explicitly calculates the SV formed by the self-motion at each discrete position. Fortunately, these SVs are similar and can be easily described. The proposed method does not need to implement multiple discrete collision detection at every discrete position to significantly reduce the computational cost.

https://doi.org/10.1017/S0263574720001393 Published online by Cambridge University Press

4. Feasibility Evaluation of Cartesian Trajectory

4.1. Approach

When the feasible arm configuration of the given tip position is empty, the manipulator cannot achieve the specified tip position. Then, based on this idea, a novel evaluation method has been developed for determining the feasibility of the Cartesian trajectory of the S-R-S-redundant manipulator under multiple constraints.

First, whether the corresponding elbow joint exceeds its limit along the given Cartesian trajectory is determined. If it is exceeding its joint limit, the Cartesian trajectory exceeds the workspace.
Second, if the feasible arm configurations Ψ_f at any position in the Cartesian trajectory are empty, the specified tip pose is never achieved within the joint limits or collision avoidance criteria; as a result, the trajectory is invalid.
Third, whether the manipulator satisfies the traversed condition between the two-arm configuration regions is determined. If the condition is satisfied, the corresponding parts of the Cartesian trajectory for the two-arm configuration regions are valid. Otherwise, only the part of the trajectory for the current arm configuration region is valid.

4.2. Traversed condition between arm configuration regions

According to the definition of an arm configuration region, when there is a transition between arm configuration regions, joint 2 or joint 6 has crossed zero during the movement. Thus, a traversed condition, whether there is a transition arm angle ψ_{ci} satisfying (20) the overlap between the two-arm configuration regions, can be obtained so that joint 2 or joint 6 simultaneously tends toward zero at the transition point to guarantee continuous movement of the manipulator.

$$1 = a \sin \psi_{ci} + b \cos \psi_{ci} + c \ (i = 2, 6) . \tag{20}$$

5. Human-like Redundancy Resolution Optimization with Multiple Constraints

5.1. Selection of optimal arm configuration region

The feasible arm configurations Ψ_f are considerably complex and may be dispersed. The selection of an optimal arm angle in Ψ_f is a very challenging task. Inappropriate optimization may lead to motion discontinuities and insufficient reachable regions.

In the previous section, the arm configuration region is introduced to further determine the unique inverse solution. The range in which the manipulator can move along Cartesian trajectories depends on the size of the selected arm configuration region; thus, a continuous and large arm configuration region should be selected. At the same time, the arm angle parameter should be optimized as much as possible in the arm configuration region to prevent motion discontinuities caused by transitions between arm configuration regions.

5.2. Human-like motion optimization

Most of the human-like optimization criteria mentioned above can be adapted to our framework. As an example, the manipulability ellipsoid optimization method is used to obtain the human-like arm configuration in our framework. The compatibility index is defined as the weighted sum of the square of the velocity transmission ratio and square of force transmission ratio. The manipulator performance achievable in the task is maximized by optimizing the compatibility index. Thus, the redundancy resolution problem of the manipulator with multiple constraints is restated as a problem of searching for the arm angle that maximizes the index in the arm configuration region. Furthermore, to guarantee continuous movement, the change rate of the arm angle cannot exceed a maximum velocity $\dot{\psi}_{\max}$, and the feasible arm configurations are further restricted. ψ' is the arm angle of the manipulator in the (m-1)th control cycle, and all feasible arm configurations Ψ_{fm} in the mth control cycle are given by

$$\Psi_{fm} = [\psi_m^l, \psi_m^u] = [\psi' - \dot{\psi}_{\max} dt, \psi' + \dot{\psi}_{\max} dt] \bigcap \Psi'_{rk}, \tag{21}$$

https://doi.org/10.1017/S0263574720001393 Published online by Cambridge University Press

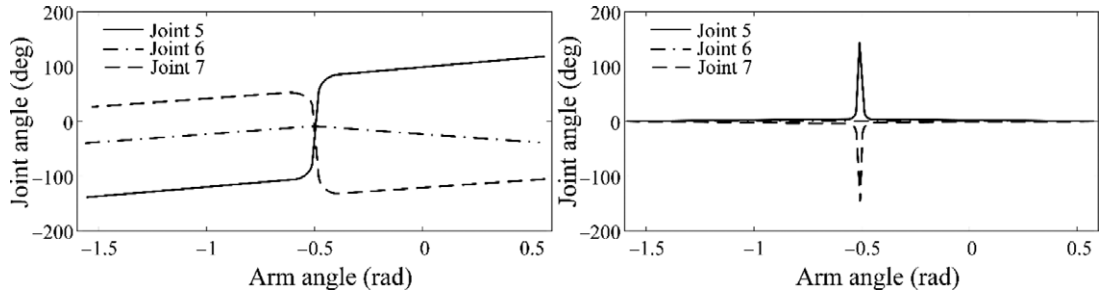

Fig. 4. The change and the change rate of joint angles 5, 6, and 7 with respect to the arm angle near the transition point.

where dt is the time interval of the control cycle and Ψ'_{rk} is the arm configuration region selected in Section 5.1. The optimal arm angle ψ'' in the mth control cycle is calculated iteratively by the following steps:

- Set the arm angle $\psi'' = \psi''_m$, set $d\psi = 0.5°$;
- For a given arm angle ψ'', we compute the inverse kinematics solutions according to the kinematic equations and then calculate the compatibility index;
- Set $\psi'' = \psi'' + d\psi$ and repeat (b) until $\psi'' > \psi''_m$;
- Find a value for ψ'' that corresponds to the maximum value of the compatibility index.

The boundaries of the arm configuration region may yield large changes in the arm angle, which leads to $\Psi_{fm} = \emptyset$. Self-motion is introduced to solve the problem. In daily life, people often adopt this strategy to change their arm configuration so that their hands can reach a more distant location.

5.3. Transition between two-arm configuration regions

Differentiating the kinematic Eqs. (3) and (9) with respect to the arm angle yields the change rate of the joint angles with respect to the arm angle. A high change rate may also cause large changes in the joint angles, and the change rate should be addressed to ensure continuous movement of the manipulator. Our analysis shows that a high change rate generally occurs near the transition point, as shown in Fig. 4. Thus, the previous approaches likely generate discontinuous motion near the transition point. To achieve the transition between arm configuration regions, the optimal arm angle needs to satisfy the following two conditions:

First, the optimal arm angle must satisfy the traversed condition between the two-arm configuration regions and pass the transition point. Second, the optimal arm angle must prevent sudden large-scale changes in joint angles caused by the high change rate. Thus, the arm angle for which the corresponding cosine type joint (joint 2 or joint 6) is the closest to zero is selected as the optimal arm angle near the transition point. Finally, we compute the redundancy resolutions of the manipulator according to the obtained optimal arm angle.

6. Experiments

6.1. System setup

Experiments were performed in our lab with a humanoid robot, which has 49 DOF.[42] The humanoid robot is composed of a mobile base, a 2-DOF waist, a 3-DOF head, two 15-DOF HIT-DLR dexterous hands, and two 7-DOF S-R-S redundancy manipulators. The link parameters of the manipulators and the joint limits are listed in Table I. It uses a control structure with an upper computer and a lower computer. The lower computer is used to control all the joints and acquire sensor data in the 2 ms control cycle. The manipulators use a position controller, and the dexterous hands use an impedance controller. The upper computer is a computer with an Intel Core 2 Duo Processor E7500 (2.93 GHz) and 8G DDR2. A kinematic control procedure executed on the upper computer is encoded by C++ and OpenInventor, with a control cycle of 100 ms. The proposed framework is implemented on the upper computer.

https://doi.org/10.1017/S0263574720001393 Published online by Cambridge University Press

Table I. Link parameters of redundant manipulator and movable ranges.

Joint	θ_i(°)	α_i(°)	**a**	**d (mm)**	**Movable ranges** (°)
1	0	−90	0	0	[−45, 175]
2	−90	90	0	0	[−105, 85]
3	0	−90	0	−400	[−115, 115]
4	0	90	0	0	[0, 125]
5	0	−90	0	−285	[−115, 115]
6	0	90	0	0	[−85, 85]
7	0	0	0	−300	[−115,115]

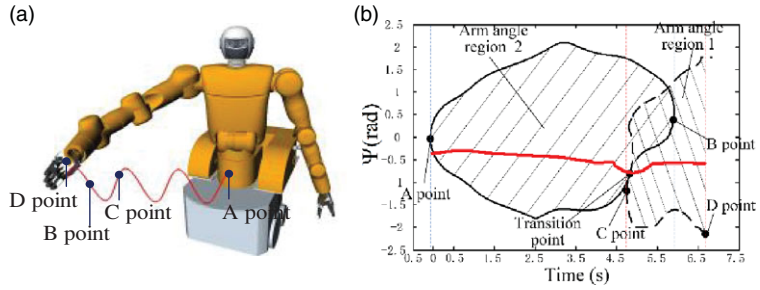

Fig. 5. The sine trajectory of the manipulator tip; (b) the feasible arm configurations along the sine trajectory and the optimal arm angle.

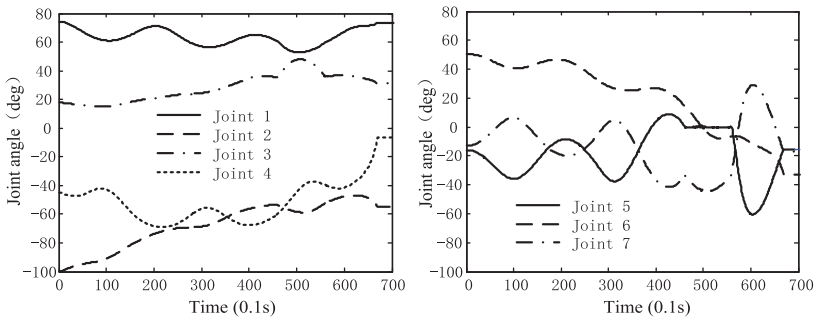

Fig. 6. The corresponding inverse kinematic solutions of the optimal arm angle.

When the computation time is shorter than the control cycle, real-time control and planning of the manipulators can be ensured. The upper computer and the lower computer use LAN communication.

6.2. Feasibility evaluation of Cartesian trajectory and transition between arm configuration regions

The desired Cartesian trajectory of the manipulator tip is a sine trajectory (Fig. 5(a)). With the same orientation of the tips, the feasible arm configurations along the trajectory include two-arm configuration regions. The part of the trajectory corresponding to arm configuration region 1 is from point C to point D, while the part of the trajectory corresponding to arm configuration region 2 is from point A to point B. The corresponding elbow joint exceeds its limit at point D. There is a transition point in the overlap of the two-arm configuration regions; thus, the whole trajectory is feasible. In Fig. 5(b), the red thick line shows the obtained optimal arm angle, which satisfies the transition conditions of the two-arm configuration regions. Figure 6 shows the corresponding redundancy resolutions. These joint angles are continuous and meet the requirements of the joint limits and collision avoidance criteria.

6.3. Human-like motion under multiple constraints

The right arm of humanoid robot moves from its rightmost position to the leftmost position in the horizontal direction to draw a straight line. A cylindrical obstacle, whose height and radius are 890 mm and 32 mm, respectively, is placed on the right side of the humanoid robot, as shown

https://doi.org/10.1017/S0263574720001393 Published online by Cambridge University Press

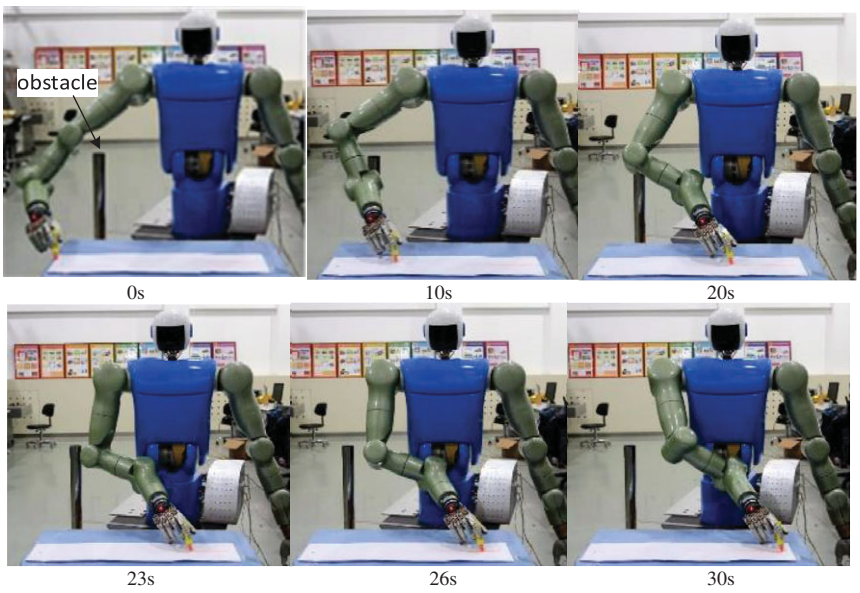

Fig. 7. Hardware system of the HIT's humanoid robot is used for experimental application and the human-like arm configurations of HIT's humanoid robot in the motion process.

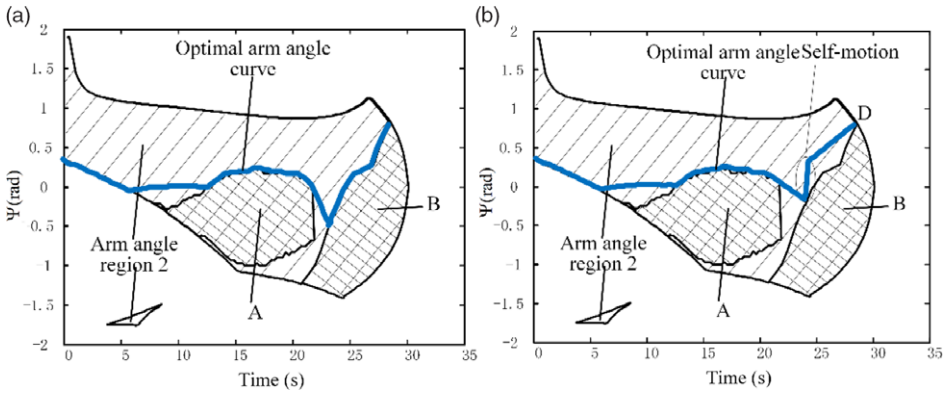

Fig. 8. The set of feasible arm configurations under joint limits and collisions constraints and the optimal arm angle curves at different maximum arm angle velocities. (a) The maximum arm angle velocity is $20°/s$. (b) The maximum arm angle velocity is $6.67°/s$.

in Fig. 7. The manipulator is restricted by the joint limits, self-collisions, and collisions with the obstacle. If only the joint limit constraint is considered, the feasible arm configurations along the trajectory consist of four-arm configuration regions. The ranges of motion corresponding to arm configuration region 2 is maximal; the maximum reachable position toward the right is [543.95, 473.49, -367.34] mm, and the maximum reachable position toward the left is [543.95, 473.49, 533.75] mm. Thus, arm configuration region 2 is selected as the optimal arm configuration region.

When the collision constraint is considered, the SV of the manipulator is composed of six SSCHs containing five vertices at a given tip position. More than 100 collision check pairs need to be checked. The average computational time for collision detection is 0.976 ms. The new feasible arm configurations are shown in Fig. 8. The shaded part in A is the arm configuration that leads to collisions between the manipulator and the obstacle, while the shadowed part in B is the arm configuration that leads to self-collisions of the humanoid robot. Considering the horizontal axis in Fig. 8, although the cylindrical obstacle and self-collision conditions yield two unfeasible arm configuration regions, the remaining arm configuration region remains continuous; thus, the manipulator can avoid collisions to complete the primary task. Due to the self-collision between the manipulator and the humanoid robot's waist, the maximum reachable position of the manipulator tips reduces to [543.95, 473.49, 458.66] mm.

https://doi.org/10.1017/S0263574720001393 Published online by Cambridge University Press

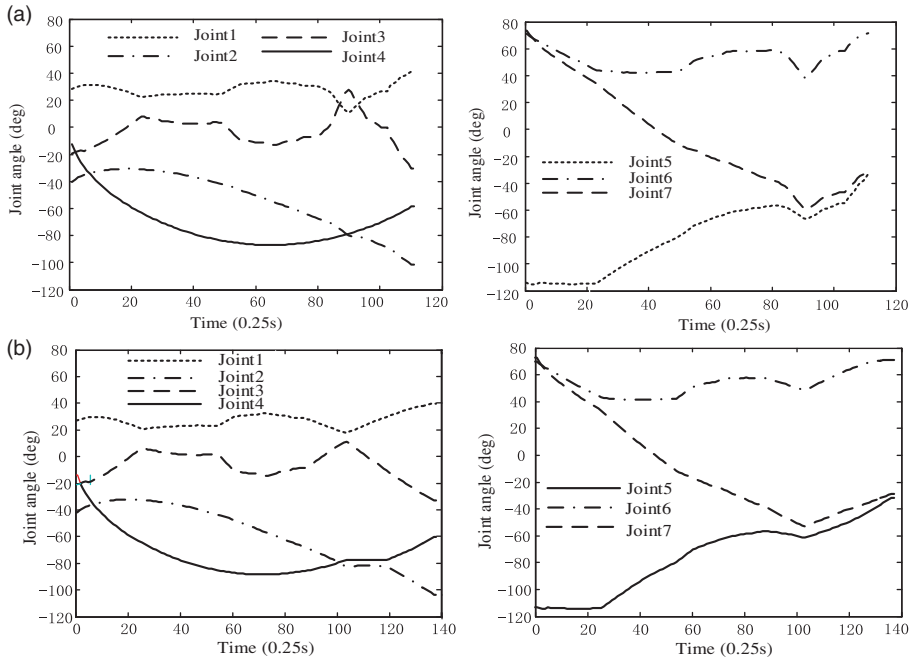

Fig. 9. Inverse kinematic solutions at different arm angle velocities. (a) The maximum arm angle velocity is $20°/s$. (b) The maximum arm angle velocity is $6.67°/s$.

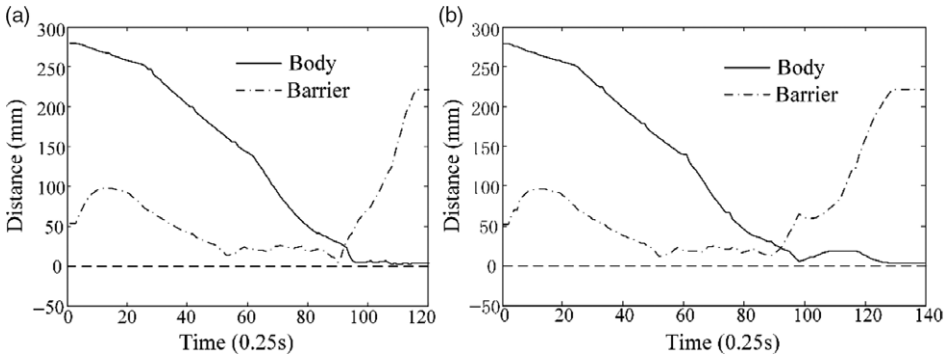

Fig. 10. The shortest distances between the manipulator and robot itself as well as the obstacle. (a) The maximum arm angle velocity is $20°/s$. (b) The maximum arm angle velocity is $6.67°/s$.

It is expected that a feasible arm angle that maximizes the compatibility index for accurate control of vertical force and horizontal velocity in this experiment can be found. The compatibility index for this task is given by

$$c = w_1 \left[u_1^T (J J^T) u_1\right]^{+1} + w_2 \left[u_2^T (J J^T)^{-1} u_2\right]^{+1}, \tag{22}$$

where $u_1 = [0\ 0\ 1]^T$, $u_2 = [1\ 0\ 0]^T$, and $w_1 = w_2 = 1$. The "+" sign is used to indicate the directions of interest. Assume that the maximum arm angle velocity $\dot{\psi}_{\max}$ is $20°/s$; the blue thick line in Fig. 8(a) corresponds to the final optimal arm angle curve. Fig. 9(a) depicts the corresponding inverse kinematic solutions of the curve. The shortest distances between the manipulator and humanoid robot itself as well as the obstacle during the experiment are shown in Fig. 10(a). The shortest distances have been maintained in a safe range to ensure that the manipulator can avoid multiple collisions and joint limits and reach the target position along the desired trajectory. Figure 7 shows the arm configurations of the humanoid robot when the arm is moving. The best arm configuration resembles that of the human arm when it is writing. Figures 8(b), 9(b), and 10(b) describe the corresponding experimental results when the maximum arm angle velocity $\dot{\psi}_{\max}$ is $6.67°/s$. Compared with the previous experiment, at the boundary of the arm configuration region, $\Psi_{fm} = \emptyset$, self-motion is introduced to

https://doi.org/10.1017/S0263574720001393 Published online by Cambridge University Press

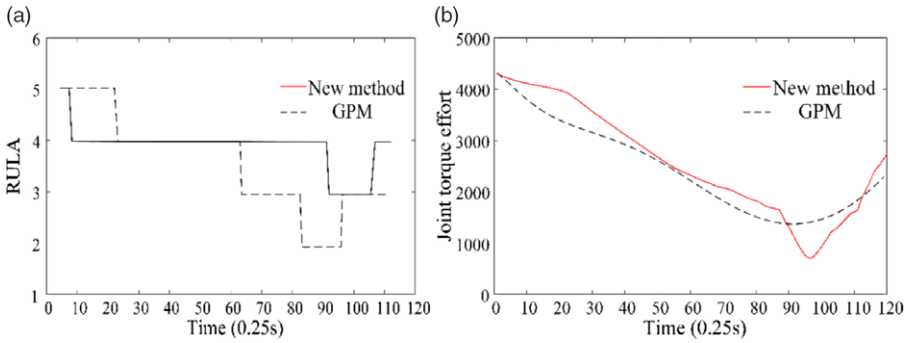

Fig. 11. (a) RULA scores for manipulator configurations of the new method with the GPM considering joint limits; (b) the torque effort values of the new method and the GPM considering joint limits.

solve this problem (see Fig. 8(b)). However, introducing self-motion increases the execution time of the whole task, and the execution time is 7 s longer than the previous time.

Rapid upper limb assessment (RULA) and a torque effort criterion are used to evaluate the similarity of the manipulator configuration with the human arm. RULA is a survey method for fast and easy evaluation of ergonomic conditions at manual workplaces.[43] RULA introduces a scoring system that investigators can employ for a selection of possibly critical work postures to assess the resulting stresses and strains on the human musculoskeletal system. RULA has proved a reliable tool for those whose job is to undertake workplace assessments. It can be used as a screening tool or incorporated into a wider ergonomics assessment of epidemiological, physical, mental, environmental, and organizational factors. Furthermore, RULA is also used to determine human-like arm postures for humanoid robot under the assumption that natural and convenient human arm postures try to avoid stresses and strains and thus feature good RULA scores.[14,44] More details regarding RULA can be found in 43,44. Figure 11(a) shows the results of the comparison between our proposed method and the GPM considering joint limits, wherein the new method has a lower RULA score, indicating an ergonomically better posture. At the same time, the results of the human motion analysis based on the musculoskeletal models show that humans exploit the strategy of muscular effort minimization to adjust the body configurations to maximize the transmission of the muscles' tension into the forces that the task requires.[45,46] Thus, a criterion of muscular effort minimization has been introduced to analyze natural human motion.[45] The muscle effort criteria U can be expressed as follows:

$$\begin{aligned} U(q) &= \|\alpha_0\|^2 = \Gamma^T (K_\Gamma K_\Gamma^T)^{-1} \Gamma \\ \alpha_0 &= K_\Gamma^+ \Gamma = K_\Gamma^T (K_\Gamma K_\Gamma^T)^{-1} \Gamma \end{aligned} , \tag{23}$$

where K_Γ is the muscle torque-activation gain matrix and K_Γ^+ is the pseudoinverse of K_Γ; Γrepresents the joint torques in terms of muscle action. This means that the most comfortable arm configuration has the minimum muscle effort under the same generalized operational space force condition. However, the muscle effort criteria cannot be used directly to determine the human-like configuration of manipulators. From the view of mechanics, the muscles of the human arm produce tensions to balance the torques of the arm joint, which is similar to the motor torque of manipulators. Thus, a torque effort criterion[47] for the manipulators is introduced as the human-like criteria to evaluate the motion similarity of the manipulator with the human arm, and is defined as follows:

$$\begin{aligned} W(q) &= \|\tau\|_2 = \left\|\tau_{posture} + \tau_{task}\right\|_2 \\ \tau_{posture} &= A(q)\ddot{q} + b(q, \dot{q}) + g(q) \\ \tau_{task} &= J_t^T F \end{aligned} , \tag{24}$$

where τ is the 7×1 vector of joint torques, $\tau_{posture}$ is the joint torques required to run the robot, and τ_{task} is the joint torques generated by an external force F;$A(q)$ is the mass matrix of the manipulator, $b(q, \dot{q})$ is the centrifugal and Coriolis terms of the manipulator, and $g(q)$ is the gravity term. Figure 11(b) shows the torque effort values of the new method and the GPM considering joint limits, wherein the new method has a higher score at the beginning due to obstacle avoidance, and a lower score after

https://doi.org/10.1017/S0263574720001393 Published online by Cambridge University Press

Table II. Comparative results between the proposed method and the existing methods.

Methods	Joint limit avoidance	Collision avoidance	Human-like motion	Consistent and continuous	Trajectory evaluation	Singularity avoidance	Average computing time (ms)	DOF
ASM	✓			✓		✓	7.563 (C++)	7
HMPIP		✓	✓	✓			41.26 (C++)	4
HMPIC			✓	✓			0.954 (C++)	4
HMS	✓	✓		✓			357.3(MATLAB)	7
GPM	✓			✓			1.432(C++)	7
Our method	✓	✓	✓	✓	✓	✓	24.83 (C++)	7

avoiding obstacles. The motion trajectories of the manipulator generated by the proposed method are more similar to those of humans.

6.4. Comparison of the proposed method with other IK-based motion generation methods

To test the efficiency of the proposed method, a comparative experiment with the existing methods is presented in this section. Two numeric solving methods and three analytical solving methods are compared in this experiment. The three analytical solving methods are the analytical solving method based on the global configuration and the arm angle parameters (ASM),[48] the human-like motion planning method based on the intrinsic principles of human arm motion (HMPIP),[47,49] and the human-like motion planning method based on arm's inherent characteristics (HMPIC).[50,51] The two numeric solving methods are the gradient projection method (GPM)[21] and the hybrid multi-objective scheme (HMS)[37]proposed by Dechao Chen. These algorithms are applied to the planning experiment in Section 6.3, to solve the IK problem at each waypoint along the test trajectory and to export the computing time, with each method repeating five times and the average computing time is regarded as the average computing time for calculating one point. These algorithms are implemented in MATLAB and C++, and are tested in a computer running Window 10 (Intel Core2 Duo E7500 at 2.93GHz, 8GB of RAM). The computing results are shown in Table II. From the results, it can be known that the proposed method is the only approach satisfying all the planning objectives.

The average computational time of the framework is 24.8306 ms; the average computational time of all feasible solutions under multiple constraints is 22.5636 ms, the average time of feasibility evaluation for the desired trajectory is 0.3205 ms, and the average time of redundancy resolution optimization is 1.942 ms. Although ASM has a faster calculation speed, it only computes a local self-motion manifold without considering the transition between local manifolds. This will lead to the insufficiency of the reachable workspace. HMPIP and HMPIC focus on generating human-like motion of a 4-DOF anthropomorphic arm based on the arm's Inherent characteristics. Although collision-avoidance is considered in HMPIP, no specific collision detection method is given. If HMPIP adopts the traditional collision detection method based on convex hulls, when the collision detection algorithm is called once for every 2° change in the arm angle, the average computational time of each waypoint is 40.13 ms in the experiment. However, the new method only needs 0.976 ms, which significantly reduces the computational time of collision detection. The numeric solving methods exhibit several disadvantages when compared to the new method-computationally more expensive; difficult to map joint limits or configurations in the velocity domain, and to handle multi-objective optimization.

This framework only applies to a pre-planned trajectory human-like motion generation. The pre-calculated trajectory is discretized into multiple waypoints, which are stored in a multidimensional array in the program. The number of waypoint depends on the duration of the trajectory. Generally, a 10-second trajectory contains 100 waypoints and requires about 2.74 KB of memory space.

7. Conclusion

In this paper, we present a general unifying framework for human-like motion control of 7-DOF S-R-S-redundant manipulators with multiple constraints. The new framework simultaneously accomplishes five objectives: Cartesian trajectory tracking, obstacle avoidance, joint limit avoidance,

https://doi.org/10.1017/S0263574720001393 Published online by Cambridge University Press

human-like movement, and evaluation of the trajectory. The existing methods are difficult to achieve these objectives at present. It is well known that each additional constraint condition in motion planning will greatly increase the difficulty of planning, and even lead to the failure of planning. At the same time, the five constraints must be considered in the motion planning of manipulators in daily life. Therefore, the general unifying framework plays an important role in the human-robot interaction and motion planning of 7-DOF-redundant manipulators.

The underpinning of our framework is a feasible arm configuration representation of an S-R-S-redundant manipulator under joint limits and obstacle constraints. Compared with the previous studies,[28,31,33] a more straightforward method for obtaining feasible arm configurations under joint limits and a modified collision detection method have been developed to compute all feasible arm configurations of a given trajectory under multiple constraints. This modified collision detection method combines discrete collision detection and continuous collision detection, as it computes the swept volumes of self-motion and represents them by SSCHs to greatly reduce the computational requirements of collision detection.

To our knowledge, this is the first study to use feasible arm configurations to quickly evaluate the feasibility of a desired Cartesian trajectory of 7-DOF-redundant manipulators under multiple constraints. The new method does not require pre-computations and builds a database for the workspace of redundant manipulators used in the previous studies.[10]

In our framework, the redundancy resolution problem of 7-DOF redundant manipulators with multiple constraints is simplified to a 1D optimization problem by using feasible arm configurations. Human-like behavior in addition to joint limits and collision avoidance constraints is used for the optimization of the inverse kinematics, so the inverse kinematics can be calculated through an efficient analytical scheme and can realize the human-like kinematic control of the S-R-S-redundant manipulators.

Although the computational time of the framework is longer than that of common IK methods, the framework can deal with more constraints and can better solve the actual motion planning problem. Furthermore, the lean structure of the framework can be run in real time with minimal computational effort and deterministic runtime. Our results are of great importance for human–robot interaction and human–robot collaboration of 7-DOF-redundant manipulators.

Despite the promising results, our study contains several limitations. This framework adopts the manipulability ellipsoid optimization to determine the human-like arm configuration, which increases the computational requirements of the algorithm. Therefore, we will further study machine learning methods to train the human arm configuration model and apply them to this framework.

Acknowledgments

The work was supported by the State Key Laboratory of Robotics and System (HIT), the National Natural Science Foundation of China (NSFC) (Grant No.51705412, No. 51975468), the Postdoctoral Science Foundation of China (Grant No. 2019M653695), and the Natural Science Foundation of Jiangsu Province (BK20191424).

Supplementary material

To view supplementary material for this article, please visit https://doi.org/10.1017/S0263574720001393.

References

1. B. Henze, R. Balachandran, et al., "Passivity analysis and control of humanoid robots on movable ground," *IEEE Rob. Autom. Lett.* **3**(4), 3457–3464 (2018).
2. F. Zhang, J. Qu, et al., "A multi-priority control of asymmetric coordination redundant dual-arm robot," *Int. J. Humanoid Rob.* **16**(2), 1–25 (2019).
3. K. Gupta, "On the nature of robot workspace," *Int. J. Robot. Res.* **5**(2), 112–121 (1986).
4. J. A. Snyman, L. J. du Plessis and J. Duffy, "An optimization approach to the determination of the boundaries of manipulator workspaces," *ASME J. Mech. Des.* **122**(4), 447–456 (2000).
5. J. Rastegar and B. Fardanesh, "Manipulation workspace analysis using the Monte Carlo method," *Mech. Mach. Theory* **25**(2), 233–239 (1990).
6. Y. Guan, K. Yokoi and X. Zhang, "Numerical methods for reachable space generation of humanoid robots," *Int. J. Robot. Res.* **27**(8), 935–950 (2008).

7. D. Kohli, J. Spanos, "Workspace analysis of mechanical manipulators using polynomial discriminants," *ASME J. Mech. Trans., Auto. Des.* **107**(2), 209–215 (1985).
8. O. Bohigas, M. Manubens, "A complete method for workspace boundary determination," *IEEE Trans. Robot.* **28**(5), 993–1006 (2012).
9. J. M. Porta, L. Ros, O. Bohigas, M. Manubens, C. Rosales, L. Jaillet, "The CUIK suite: motion analysis of closed-chain multibody systems," *IEEE Rob. Auto. Mag.* **21**(3), 105–114 (2014).
10. F. Zacharias, C. Borst and G. Hirzinger, "Capturing robot workspace structure: representing robot capabilities," in *Proceedings of the IEEE/RSJ International Conference on Intelligent Robots and Systems* (2007) pp. 3229–3236.
11. H Kim, J Rosen, "Predicting redundancy of a 7-DOF upper limb exoskeleton toward improved transparency between human and robot," *J. Intell. Rob. Syst.* **80**(1), 99–119 (2015).
12. B. Almasri and F. B. Ouezdou, "Human-like motion based on a geometrical inverse kinematics and energetic optimization," in *Proceedings of the IEEE/RSJ International Conference on Intelligent Robots and Systems* (2008) pp. 3486–3491.
13. J. Zhao, B. Xie, C. Song, "Generating human-like movements for robotic arms," *Mech. Mach. Theory* **81**, 107–128 (2014).
14. F. Zacharias, C. Schlette, F. Schmidt, C. Borst, J. Rossmann, G. Hirzinger, "Making planned paths look more human-like in humanoid robot manipulation planning," in Proceedings of the IEEE International Conference on Robotics and Automation (2011) pp. 1192–1198.
15. T. Kang, J. He, et al., "Determining natural arm configuration along a reaching trajectory," *Exp. Brain Res.* **167**, 352–361 (2005).
16. S. L. Chiu, "Task compatibility of manipulator postures," *Int. J. Robot. Res.* **7**(5), 13–21 (1988).
17. O. Khatib, E. Demircan, V. De Sapio, L. Sentis, T. Besier, S. Delp, "Robotics-based synthesis of human motion," *J. Physiol.* **103**(3–5), 211–219 (2009).
18. P.K. Artemiadis, P.T. Katsiaris, K.J. Kyriakopoulos, "A biomimetic approach to inverse kinematics for a redundant robot arm," *Auton. Robot.* **29**(3–4), 293–308 (2010).
19. A. M. Zanchettin, L. Bascetta, P. Rocco, "Achieving humanlike motion resolving redundancy for anthropomorphic industrial manipulators," *IEEE Robot. Autom. Mag.* **20**(4), 131–138 (2013).
20. C. Klein, C. Huang, "Review of pseudoinverse control for use with kinematically redundant manipulators," IEEE Trans. Systems, Man *Cybern.* **13**(3), 245–250 (1995).
21. R. V. Dubey, J. A. Euler and S. M. Babcock, "Real-time implementation of an optimization scheme for seven-degree-of-freedom redundant manipulators," *IEEE Trans. Robot.* **7**(5), 579–588 (1991).
22. A. S. Deo and I. D. Walker, "Overview of damped least-squares methods for inverse kinematics of robot manipulators," *J. Intell. Robot. Syst.* **14**(1), 43–68 (1995).
23. T. F. Chan, R. V. Dubey, "A weighted least-norm solution based scheme for avoiding joint limits for redundant joint manipulators," *IEEE Trans. Robot. Autom.* **11**(2), 286–292 (1995).
24. S. Chiaverini, "Singularity-robust task-priority redundancy resolution for real-time kinematic control of robot manipulators," *IEEE Trans. Robot. Autom.* **13**(3), 398–410 (1997).
25. B. Siciliano, J-J. Slotine, "A general framework for managing multiple tasks in highly redundant robotic systems," in Proceedings of the IEEE International Conference on Advanced Robotics (1991) pp. 1211–1216.
26. J. Xiang, C. Zhong and W. Wei, "General weighted least-norm control for redundant manipulators," *IEEE Trans. Robot.* **26**(4), 660–669 (2010).
27. J. Xiang, C. Zhong and W. Wei, "A varied weights method for the kinematic control of redundant manipulators with multiple constraint," *IEEE Trans. Robot.* **28**(2), 330–340 (2012).
28. N. Vahrenkamp, D. Muth, P. Kaiser and T. Asfour, "IK-MAP: an enhanced workspace representation to support inverse kinematics solvers," in Proc*eedings of the* IEEE/RAS International Conference on Humanoid Robots (Humanoids) (2015) pp. 785–790.
29. B.Tondu, "A closed-form inverse kinematic modelling of a 7R anthropomorphic upper limb based on a joint parametrization," in *Proceedings of the IEEE/RAS International Conference on Humanoid Robots* (2006) pp. 390–397.
30. Martin Pfurner, "Closed form inverse kinematics solution for a redundant anthropomorphic robot arm," *Comput. Aided Geom. Des.* **47**, 163–171 (2016).
31. H. Moradi and S. Lee, "Joint limit analysis and elbow movement minimization for redundant manipulators using closed form method," Advances in Intelligent Computing, Part 2 (3645), pp. 423–432 (2005).
32. K. Kreutz-Delgado, M. Long and H. Seraji, "Kinematic analysis of 7-DOF manipulators," *Int. J. Rob. Res.* **11**(5), 469–481 (1992).
33. M. Shimizu, H. Kakuya, W. K. Yoon, et al., "Analytical inverse kinematic computation for 7-DOF redundant manipulators with joint limits and its application to redundancy resolution," *IEEE Trans. Robot.* **24**(5), 1131–1142 (2008).
34. X.L. Ding, C. Fang, "A novel method of motion planning for an anthropomorphic arm based on movement primitives," *IEEE/ASME Trans. Mechatronics* **18**(2), 524–636 (2013).
35. C. L. Lück and S. Lee, "Self-motion topology for redundant manipulators with joint limits," in IEEE International Conference on Robotics and Automation (1993) pp. 626–631.
36. W. Liu and D. Chen, "Analytical inverse kinematics solver for anthropomorphic 7-DOF redundant manipulators with human-Like configuration constraints," *J. Intell. Robot. Syst.* **86**(1), 63–79 (2017).

37. D. Chen and Y. Zhang, "A hybrid multi-objective scheme applied to redundant robot manipulators," *IEEE Trans. Autom. Sci. Eng.* **14**(3), 1337–1350 (2017).
38. Y. Zhang, S. Chen, S. Li and Z. Zhang, "Adaptive projection neural network for kinematic control of redundant manipulators with unknown physical parameters", *IEEE Trans. Ind. Electron.* **65**(6), 4909–4920 (2018).
39. O. Stasse, A. Escande, N. Mansard, S. Miossec, et al., "Real-time (self)-collision avoidance task on a HRP-2 humanoid robot," in *Proc. IEEE Int. Conf. Robot. Autom.* (2008) pp.3200-3205.
40. H. Täubig, B. Bäuml, U. Frese, "Real-time swept volume and distance computation for self-collision detection," in *Proceedings of IEEE/RSJ International Conference on Intelligent Robots and Systems* (2011) pp.1585–1592.
41. S. Redon, Y. J. Kim, M. C. Lin and D. Manocha, "Fast continuous collision detection for articulated models," *Acm Symp. Solid Model. Appl.* **5**(2), 145–156 (2004).
42. Y. Ren, Y. Liu, M. Jin and H. Liu, "Biomimetic object impedance control for dual-arm cooperative 7-DOF manipulators," *Rob. Auton. Syst.* **75**, 273–287 (2016).
43. L. McAtamney and E. N. Corlett, "RULA: a survey method for the investigation of work-related upper limb disorders," *Appl. Ergon.* **24**(2), 91–99 (1993).
44. Y. Gan, X. Dai, "Human-like manipulation planning for articulated manipulator," *J. Bionic Eng.* **9**(4), 434–445 (2012).
45. V. De Sapio, J. Warren and O. Khatib "Predicting reaching postures using a kinematically constrained shoulder model," in Proceedings of the Advances in Robot Kinematics (Springer, Dordrecht, 2006) pp. 209–218.
46. E. Demircan, A. Murai, O. Khatib and Y. Nakamura, "Muscular effort for the characterization of human postural behaviors," in Proceedings of the Experimental Robotics (2016) pp. 685–696.
47. M. Li, W. Guo, R. Lin, C. Wu and L. Han, "An efficient motion generation method for redundant humanoid robot arm based on the intrinsic principles of human arm motion," *Int. J. Humanoid Rob.* **15**(6), 1850026 (2018).
48. C. Faria, F. Ferreira, W. Erlhagen, S. Monteiro and E. Bicho, "Position-based kinematics for 7-DoF serial manipulators with global configuration control, joint limit and singularity avoidance," *Mech. Machine Theory* **121**, 317–334 (2018).
49. M. Li, W. Guo, R. Lin and C. Wu, "An efficient motion generation method for redundant humanoid robot arms based on motion continuity," *Adv. Rob.* **32**(22), 1185–1196 (2018).
50. H. Xu and X. Ding, "Human-like motion planning for a 4-DOF anthropomorphic arm based on arm's inherent characteristics," *Int. J. Humanoid Rob.* **14**(04), 1750005 (2017).
51. H. Xu and X. Ding, "Consistent point-to-point motion planning of anthropomorphic arms," *Int. J. Humanoid Robot* **4**, (2019). doi: 10.1142/S0219843619500075.